Scientific Reports

https://doi.org/10.1038/s41598-025-34645-5

Article in Press

Network centrality drives optimal protection investment against systemic risk propagation in complex systems

Received: 9 February 2025

Accepted: 30 December 2025

Published online: 19 January 2026

Cite this article as: Park C. Network centrality drives optimal protection investment against systemic risk propagation in complex systems. *Sci Rep* (2026). https://doi.org/10.1038/s41598-025-34645-5

Chulwook Park

Network Centrality Drives Optimal Protection Investment Against Systemic Risk Propagation in Complex Systems

Chulwook Park[1,2,3,*]

[1]International Institute for Applied Systems Analysis (IIASA), A – 2361 Laxenburg, Austria.
[2]Okinawa Institute of Science and Technology (OIST), m1919-1, Okinawa, Japan.
[3]Department of Physical Education, Seoul National University, 08826, Seoul, South Korea.

* BK21 Four, Associate Professor, Seoul National University. Email: pcw8531@snu.ac.kr

ABSTRACT

The aim of this study is to investigate the mechanisms underlying systemic risk mitigation in scale-free networks by modeling the roles of memorized capital, social learning, and centrality-based heuristics. The study employs a network–agent dynamic approach to examine how node centrality shapes protection decisions and vulnerability distributions. Using advanced computational methods and interactive simulations, the study systematically tracks key state variables and shows that nodes with higher centrality tend to invest more substantially in protection, indicating a positive relationship between centrality and proactive risk management. These findings provide new insights into risk propagation and highlight that local decision rules may converge to suboptimal equilibria when left uncoordinated. By demonstrating the critical role of strategic collaboration and regulatory oversight, the results outline potential pathways toward enhanced network resilience, offering both theoretical and practical contributions to systemic risk mitigation across interconnected domains.

Keywords: Systemic risk, Network–agent dynamics, Centrality, Heuristics, Protective investment

Introduction

Systemic risk, a critical concept across various fields, refers to the likelihood that localized failures or chains of such events can trigger the collapse of a larger system[1]. It highlights situations where difficulties faced by a single entity can spread throughout the system, potentially causing widespread disruption or even total failure. Events such as the 2008 global financial crisis, the COVID-19 pandemic, and cascading power grid failures like the 2003 Northeast blackout illustrate this dynamic. A defining feature of systemic risk is its interconnectedness and capacity for rapid propagation[2], meaning the failure of one component can quickly affect others and trigger cascading disruptions. Consequently, research has centered on understanding network structures, mechanisms of propagation, and strategies to reduce this spread[3].

Growing system complexity and interconnectedness have intensified interest in systemic risk. Researchers from various disciplines have developed advanced models to better capture and predict its dynamics[4,5]. This work has broadened the concept beyond finance and epidemiology to other complex systems[6]. Examples include disease outbreaks spreading through transportation networks, competitive advantages diffusing through sports leagues as teams adopt successful strategies, and technological innovations propagating through industrial ecosystems. Recent studies increasingly adopt a network perspective, emphasizing that the structure linking nodes (e.g., institutions, individuals, or countries) critically shapes how failures propagate[7,8]. This growing focus highlights the need to understand network structure and connectivity to mitigate systemic risk effectively. Systemic risk analysis offers broad applicability, providing policymakers, regulators, and stakeholders with essential insights to build systems resilient to shocks. It also supports designing policy interventions that prevent cascading failures and strengthen overall resilience[9,10].

Despite mounting evidence of systemic risk across networked health systems[11], a clear gap remains in the literature[12]: insufficient distinction between the likelihood of failure contagions and the potential for these defaults to propagate[13]. Although related, these dynamics arise from different mechanisms and require distinct modeling approaches. Estimating default likelihood centers on individual risk factors and behaviors, whereas understanding propagation depends on

network interconnectedness[14]. Studies show that many models overlook the influence of network–agent dynamics—patterns shaped by spatial and temporal heterogeneity—across systems[15,16]. Spatial heterogeneity reflects variation in network properties (e.g., node degree, clustering) across regions, while temporal heterogeneity captures evolving node states and connections over time[17]. In financial networks, spatial heterogeneity appears as variation in bank sizes and interconnectedness, while temporal heterogeneity reflects shifting lending relationships and capital levels. In epidemiological networks, spatial heterogeneity corresponds to differing population densities and contact patterns, while temporal heterogeneity reflects seasonal mobility and changing immunity levels. This oversight limits models that aim to predict failure spread in real systems and underscores the need to understand how structure and connectivity shape systemic risk propagation. To address this gap, this study examines systemic risk across diverse networks, focusing on the interplay among structure, connectivity, propagation, and individual investment in protection.

We integrate principles from graph theory into complex systems, offering a heuristic understanding of contagion dynamics and how network properties shape risk likelihood[8], to fields such as financial markets, public health, infrastructure networks, and competitive dynamics that have long drawn scholarly and policy interest[18,19]. Although system failure is often a low-probability event, its consequences can rapidly reverberate across the network[20]. This phenomenon appears when a single adverse condition triggers a domino effect that spreads widely[21]. Empirical work highlights systemic risks arising from extreme events intensified by segmented production structures. Building on these findings, our investigation examined the impact of investment, conceptualized as stochastic memorized capital with adaptive strategies—on these systems, incorporating social learning and evolutionary dynamics[22]. This perspective aligns with research emphasizing the influence of individual behaviors on resilience to isolated and systemic risks. Our model also examines the dual role of network connectivity in shaping systemic risk[4] and influencing investment decisions. Dense connections can heighten contagion likelihood, yet diversification benefits may offset this risk[5]. To evaluate the model, we simulated a random shock to an individual within the network, hypothesizing that increased connections would raise risk potential despite diversification gains.

While existing network contagion models have offered valuable insights into systemic risk propagation, they often treat protection investment as fixed or uniform across nodes, overlooking how network position shapes risk exposure and optimal protection levels. This becomes critical when highly connected nodes underinvest, creating system-wide vulnerabilities—whether in banking networks where major institutions skimp on liquidity buffers, hospital networks where central facilities underinvest in infection control, or sports leagues where dominant teams neglect injury prevention. To handle these points, our approach introduces three innovations. First, we implement a saturating protection function [$p_{\mathrm{p}} = p_{\mathrm{p,max}}/(1 + c_{\mathrm{p},1/2}/(f_{\mathrm{p}}c))$] that reflects diminishing returns on investment. Second, we propose a centrality-based heuristic ($f_{\mathrm{p}} = f_{\mathrm{p0}} + f_{\mathrm{p1}}C$) in which nodes adjust protection according to network position, with f_{p0} representing baseline protection and f_{p1} capturing centrality responsiveness. Third, we integrate memorized capital [$c_m = m_e * c_{new} + (1 - m_e) * c_{old}$] with social learning [$p_{\mathrm{i}} = 1/(1 + \exp(-s\Delta c))$], allowing adaptive strategies informed by past success. (see Methods for details). This scheme enables analysis of how local optimization interacts with networks to generate emergent outcomes, yielding insights beyond traditional models. By examining structure alongside strategic interventions and risk mitigation behaviors, we clarify systemic vulnerabilities and support the development of informed mitigation strategies for interconnected systems.

Results

Our results show how systemic risk arises and spreads through interconnected networks, with implications for financial contagion, disease transmission, and competitive dynamics in sports. Simulations indicate that centrality-based protection strategies reduce systemic vulnerability, though optimal connectivity and learning remain important considerations.

Schematic illustration of the spread of failures and protection against them

The spread of failures in complex systems is a major concern for researchers and policymakers. Understanding how failures propagate and implementing effective protective measures are essential for system stability and resilience.

Failure propagation is strongly shaped by network structure and the degree of interconnectedness among entities. To capture these dynamics, researchers have developed mechanisms that quantify the importance of variables in a network[23]. These models help identify features capable of disseminating failures and clarify propagation patterns. As illustrated in Fig. 1, the spread of failures depends on interconnectedness, the balance between failure probability and protection potential. Failures can be mitigated through interventions (such as vaccination in disease networks) that lower failure probability or strategies (such as diversification in financial systems) that enhance protection potential[18,19]. Understanding these fundamentals is essential for strengthening resilience in interconnected systems.

Failures across various network structures

The simulation results in Fig. 2 show how failures propagate across network types with distinct vulnerability patterns under full connectivity (0–100). Random (Erdős–Rényi), regular, small-world (Watts–Strogatz), and scale-free (Barabási–Albert) networks exhibit differing responses to systemic risks. Visualizations present node and link failures as cumulative or isolated events per degree. Random networks show resilience that shifts with network parameters. Regular networks, defined by uniform connections, can amplify systemic risks unless critical density is reached. Small-world networks, with high clustering and short path lengths, initially localize failures but later permit rapid propagation. Scale-free networks, shaped by power-law degree distributions, emphasize the role of hubs—vulnerable to targeted attacks yet robust against random failures.

Examining network structures reveals varied responses to failures. Although failure potential increases across all topologies, scale-free networks respond more rapidly under similar failure probabilities [node failure (p_n) and link failure (p_l)] at low connectivity degrees[24]. This mirrors real systems: financial networks concentrate risk in highly connected institutions, airline networks rely on hubs where disruptions cascade, disease transmission is driven by super-spreaders, and tactical innovations in sports diffuse from dominant teams. These parallels motivate further analysis of scale-free networks.

Illustration of conditions maximizing the failure probability in scale-free networks

Centrality in this context relates to the initial network property values (i.e., $\mathrm{G}[n, m]$). According to our model's operational principle (see Methods), localized failures can escalate into system breakdowns. At each time step, every node faces a failure probability p_{n} , and this failure can propagate along each link with probability p_{l}, driving systemic contagion. Simulations revealed a strong correlation between contagion and the node with the highest eigenvector centrality[14] (see Appendix 1, Table S1, Table S2, and Fig. S1). For example, infection (1) first occurred at node 5, which had the highest centrality (Table 1).

Table 1. Numerical results for eigenvector centrality in a scale-free graph of $n = 10$ nodes with m expected degrees.

$nodes\ (n)$	0	1	2	3	4	5	6	7	8	9
$eigenvector\_centrality$	0.21	0.22	0.21	0.22	0.22	0.45	0.42	0.39	0.35	0.32
$contagion\ (failure)$	0	0	0	0	1	1	1	1	1	1

Note: Values were obtained from the simulation with the failure states between failed (1) and not failed (0).

We examined an intermediate degree of connectivity that heightens a network's contagion potential, drawing on centrality effects and the "rich-get-richer" phenomenon[25]. Because our model can run under conditions where $f_{\mathrm{p0}} = f_{\mathrm{p1}} = 0$ (no strategy evolution), we validated this by illustrating average failure probability as a function of connectivity and observing emerging trends. This search aimed to identify patterns consistent with prior studies on contagion in financial networks[21]. We hypothesized that identifying a connectivity value that maximizes failure would provide a strong candidate for initializing parameters in our evolutionary dynamics.

Table 2. Numerical results for connectivity in a scale-free graph of $n = 100$ nodes with m expected degrees.

$degree\ (m)$	1	2	⋯	10	20	⋯	40	50	⋯
$fail.prob$	0.292	0.589	⋯	0.990	0.999	⋯	0.999	0.999	⋯
$me.capi$	3.023	1.671	⋯	1.008	1.000	⋯	1.000	1.000	⋯

Note: Values were obtained under these conditions: network = scale-free graph, number of nodes = 100, number of connections per node = 1–99 ($fail.prob$=*failure probability*, $me.capi$= *memorized capital*), and time steps = 100,000 (periods 1–100,000).

Our analysis produced notable observations (Table 2, Fig. 3.1): a peak emerged at approximately 10% connectance, forming a plateau between low and high connectivity levels. Connectance refers to the ratio of actual connections to the theoretical maximum number of links in the network (see Appendix 2, Table S3, Fig. S2 and S3 for details). To validate selecting 10% connectance for subsequent analyses, we conducted simulations across the full connectivity range. All four network topologies, random, regular, small-world, and scale-free, exhibited a consistent threshold near 10% connectivity. Below this threshold, failure probability increased sharply as isolated nodes became integrated into the network. Beyond this point, failure probability plateaued, indicating diminishing returns for cascade propagation. The consistency across structurally distinct networks, from the uniform degree distribution of regular networks to the heavy-tailed distribution of scale-free networks, demonstrates that the 10% threshold arises from the interaction between local failure propagation (governed by p_l) and overall network connectivity, independent of specific structural properties. Although this threshold may shift under different conditions, such as alternative model parameters or varying network sizes, it aligns with real-world patterns. Epidemiological studies indicate that outbreaks become self-sustaining when infected individuals contact about 10% of their community, and research on innovation diffusion reports a comparable tipping point for adoption.

Excluding self-links, the number of possible connections equals the product of nodes and one less than nodes, divided by two. This suggests an optimal connectance of ~ 0.1, which provides meaningful interaction potential yet creates challenges for the social evolution of preventive measures. For systemically important institutions, capping direct exposures at about 10% of participants, similar to limits in banking regulation, is recommended. Rather than allowing unchecked hub growth, regulators could require segmentation once thresholds are reached. In public health, this corresponds to limiting gathering sizes to 10% of a community during outbreaks. In sports, leagues may likewise restrict direct competition (e.g., divisional play) to 10% of teams to balance exposure and stability. Our findings support tiered network designs where regional subsystems maintain ~10% internal connectivity and link more sparsely to global hubs, mirroring regional payment processing. As systems expand, sustaining 10% connectance requires active management, revealing natural limits to scaling without hierarchical organization. These results clarify how connectivity can both amplify and suppress failure spread while altering failure likelihood.

Interplay of centrality-based heuristics

Observations in Fig. 3.2 show that social learning parameters strongly shape system dynamics. Moderate imitation probability (i.e., p_r = 0.1) yields superior long-term outcomes, producing lower average failure rates than other values. This result indicates that excessive imitation spreads suboptimal strategies, whereas moderate learning maintains strategy diversity and local optimization. Similar patterns appear across domains: financial institutions that mimic competitors indiscriminately often fail together, while selective adaptation promotes resilience. In epidemic control, communities that moderately adopt others' prevention measures perform better than those with rigid or chaotic responses. We examined the effects of evolutionarily informed parameters, memory, imitation (p_r; see Appendix 3, Fig. S4 and S5 for more details), and exploration (p_e; see Appendix 4, Fig. S6.1–S10.3 for the details) on failure probability. High parameter values accelerate social evolution, while low values slow adaptation. Simulations predict an intermediate minimum failure probability for these social variables, consistent with a complex system shaped by multiple interacting factors.

Table 3: Numerical results for eigenvector_centrality [$Ax = \lambda x$].

$node(i)$	0	1	⋯	10	11	⋯	50	51	⋯	75	76	⋯	98	99
$value(\lambda x)$	0.24	0.10	⋯	0.12	0.22	⋯	0.08	0.09	⋯	0.08	0.06	⋯	0.04	0.04

Note: Eigenvector_centrality was obtained from the left-hand side of Fig. 4; type of network = scale-free (Barabási–Albert model), number of nodes = 100, number of connections per node = 10.

Fig. 4.1 illustrates the relationship between an agent's centrality (Table 3) and investment in protection. Each point represents an individual: color denotes centrality, and vertical position reflects protection investment (see Appendix 5.1, Supplement Fig. S11.1 ~ S11.3 for more cases). The simulations show that agents with higher eigenvector centrality invest more in protection. Eigenvector centrality, calculated via the power method, measures global network connectivity. Agents with greater centrality, due to their broader influence and faster information flow, are more likely to invest. To test the heuristic's robustness, we compared it with alternative strategies. Fig. 4.2 shows that network-aware strategies outperform random allocation, uniform protection, and degree-, betweenness-, and closeness-based approaches (Appendix 5.2, Fig. S12 and S13 for the details). We then extended simulations to track long-term failure stabilization and evaluate the dynamics of the adopted strategy, incorporating three key adjustments.

Table 4: Numerical results for eigenvector_centrality [$Ax = \lambda x$].

$node(i)$	0	1	⋯	10	11	⋯	50	51	⋯	75	76	⋯	98	99
$value(\lambda x)$	0.08	0.13	⋯	0.32	0.21	⋯	0.08	0.07	⋯	0.06	0.05	⋯	0.05	0.05

Note: Eigenvector_centrality was obtained from the left-hand side of Fig. 5; type of network = scale-free (Barabási–Albert model), number of nodes = 100, number of connections per node = 10.

Fig. 5 illustrates the relationship between eigenvector centrality (Table 4, Appendix 6 for ordering by eig_centrality [node]) and protection investment (top panel: n = 1000, m = 100; bottom panel: n = 100, m = 10). Semi-transparent lines track the evolution of selected individuals over time, and an additional panel examines the interaction among eigenvector centrality, failure rates, and strategic dynamics. Our proposed heuristic, $f_{\mathrm{p}} = f_{\mathrm{p0}} + f_{\mathrm{p1}} C$, is depicted visually, showing that nodes with higher centrality invest more in protection. Ordering nodes by centrality highlights the slope and intersection of this relationship. Regression analysis yields an R^2 value (0.987) for f_{p}, confirming strong significance and validating the heuristic across contexts. Analogous to how major banks hold higher capital reserves, central hospitals maintain surge capacity, key infrastructure nodes require redundancy, and star athletes receive enhanced injury prevention, systemic importance necessitates proportional protection. Directional strategy effects, with f_{p0} = negative and f_{p1} = positive, offer insight into micro-scale interactions between failure and protection. Importantly, the strong centrality–protection correlation emerges from system dynamics rather than model specification. As shown in Supplementary Appendices 3–6, this pattern appears only under specific conditions: moderate imitation (p_r), moderate exploration (p_e), and sufficient memory (m_e). Under alternative settings—particularly high exploration noise (σ_e) or low memory and imitation rates (p_r)—the system exhibits diverse outcomes, including negative f_{p1} values (inverse centrality relationship) or near-zero R^2 values (no systematic relationship; Supplement Fig. S11.3). These findings demonstrate that the model genuinely explores strategy space, with centrality-based protection becoming the evolutionarily stable strategy only when agents can reliably evaluate and imitate successful strategies (see Appendix 7 for more validation).

Empirical calibration and validation

Fig. 6.1 compare phase portraits under different sigma values, linking model behavior to real-world scenarios (reflecting parameter values from Fig. 5). The portraits show a predominantly positive relationship between f_{p0} and f_{p1}, indicating that nodes with higher eigenvector centrality tend to invest (f_{p}) more in protection, consistent with Fig. 5. The exploration mechanism, influenced by the sigma value (σ_e), is central to this shift. Agents with probability p_{e} adjust one of their strategy values (f_{p0} or f_{p1}) by a normally distributed increment with mean 0 and standard deviation σ_e, reflecting their propensity for experimentation or responses to environmental changes. Higher randomness disrupts the synchronization seen in deterministic settings, producing scattered, anti-synchronized dynamics.

Fig. 6.2 further illustrates how f_{p0} and f_{p1} respond to varying noise levels σ_{e}. Notably, f_{p1} remains relatively stable at low to moderate σ_{e} values (e.g., 0.0001 up to 0.1), whereas f_{p0} varies more, with the horizontal line rising as σ_{e} increases.

This shows that f_{p0} is more sensitive to stochastic shifts in agent strategies, while f_{p1} maintains steadier trajectories under moderate noise. These noise-sensitivity patterns have practical implications. Systems with low exploration noise maintain stable protection strategies, such as mature financial markets with established regulations or disease management under routine protocols. High-noise environments, such as emerging markets, novel outbreaks, or sports leagues with frequent rule changes, exhibit greater volatility, particularly in baseline protection levels. By overlapping vertical diagrams at selected σ_e values, we highlight stable versus unstable tendencies in f_{p1}. When σ_e remains small, the vertical arrows converge to a stable point, reflecting synchronized protection investments. In contrast, a hypothetical "$\sigma_e = 0.0$" line shows how a fully deterministic yet unstable reference can diverge when perturbed. Thus, although f_{p1} generally retains stability under moderate σ_e, f_{p0} rises with increasing noise, demonstrating how randomness in exploratory behavior amplifies one dimension of the protective strategy while leaving the other comparatively stable.

Mechanical rationalization for systemic risk management

These comparisons motivate the model mechanism (Fig. 7; see Methods for details) and affirm its relevance to real-world systems, showing that centrality's influence on protection investment persists as the system evolves While Fig. 5 and 6 indicated that highly central nodes increase protection under moderate noise, Fig. 7 illustrates network convergence toward equilibrium: central nodes maintain high protection, whereas peripheral nodes invest less. This adaptive balance reflects the model's contagion-tracking process, where heavily protected hubs act as firewalls stabilizing the failure rate. Over time, nodes align protection with centrality, as reducing investment increases individual failure risk. The lower panel shows that protection (f_p) embedded in its strategic components (f_{p0} and f_{p1}) and centrality (C) is essential for systemic stability, demonstrating how dynamic strategies mitigate propagation risk. Such self-organization appears in domains such as banking, health systems, and sports, though the resulting order may still be globally suboptimal, highlighting the need for coordinated intervention.

To connect this framework with real-world applications, we validated our centrality-based protection model using datasets from finance, epidemiology, and sports, each demonstrating distinct network-mediated risk dynamics. Fig. 8 synthesizes these findings across three perspectives. The left panel shows that our protection function $p_p = p_{p,max}/(1 + c_{p,1/2}/(f_p c))$ captures domain-specific saturation patterns in voluntary prevention adoption (see Supplementary Appendix 10, Table S11). The right panel demonstrates consistent social learning dynamics, with Fermi adoption curves producing selection strengths (s) between 0.9–1.1, suggesting behavioral mechanisms governing strategy imitation that hold across contexts. The middle panel confirms strong predictive accuracy (mean $r = 0.694$), showing that centrality-based protection strategies apply across domains, mitigating financial contagion through capital buffers, reducing disease transmission via vaccination, and preserving competitive advantage through injury prevention, thereby validating the framework's practical relevance and its Fermi learning function for systemic risk management (see Supplementary Appendix 11, Fig. S14).

Discussion

In this study, we developed a network model to examine how failures spread and how protection evolves. Our approach builds on established contagion while introducing a centrality-based heuristic that extends traditional foundations.

First, we proposed a method comparable to existing network processes for simulating risk propagation, incorporating a mechanism that distinguishes our model from prior formulations. Traditional models suggest that denser connections increase contagion risk by expanding transmission channels, meaning highly connected nodes, banks, transportation hubs, or influential individuals, have greater failure potential. Eigenvector centrality quantifies this relationship, linking risk to individual characteristics and connection patterns. Our model further shows that increased connectivity also enables risk sharing[21], mitigating failure probabilities. Simulations revealed that although connectivity raises contagion likelihood, it simultaneously introduces stabilizing effects. These findings have practical implications for financial, social, transportation, and competitive sports networks. The positive correlation between centrality and optimal protection

investment suggests that current regulatory mechanisms appropriately strengthen oversight of systemically important nodes. Furthermore, the enhanced failure probability observed at medium connectivity (≈ 10%) reflects the "robust-yet-fragile" behavior of real networks: sufficient interconnectedness supports liquidity sharing during normal periods yet accelerates contagion under stress[16]. This implies that optimal network design may require explicit constraints on maximum node degree, a concept reflected in concentration limits but not fully embedded in systemic risk policy.

Second, our research examined how individuals invest in protection, drawing on social learning principles such as imitation, exploration, stochastic influences, and the moving average effect shaping decision-making[27]. We focused on dilemmas where personal incentives can undermine collective outcomes[28,29], consistent with "the evolution of cooperation"[30]. This dynamic appears across domains: banks collaborating on stress tests[31], health systems coordinating pandemic responses[12], and sports leagues sharing injury-prevention strategies[26]. Simulations revealed that nodes with higher eigenvector centrality invest more in protection, a pattern strengthened when nodes are reordered by centrality ranking[23]. We propose strategic interventions, such as enforceable agreements that penalize harmful behavior, to strengthen cooperation and reduce dependence on mutual trust[32,33]. These findings advance understanding of failure and protection dynamics in networked systems and offer pathways for promoting cooperative risk management.

Third, recent global crises highlight the systemic vulnerabilities captured by our model. The 2008 financial crisis showed how the collapse of highly connected institutions, such as Lehman Brothers, triggered cascading failures across banking networks, requiring bailouts even for less-exposed institutions[34]. COVID-19 similarly revealed how hub hospitals became overwhelmed and how super-spreader events accelerated infections, forcing emergency reallocations of critical resources[35,36]. Both crises demonstrated that networks may appear stable yet collapse abruptly when pushed beyond critical thresholds[37]. These events support our model's predicted optimal connectivity (~10%), observed in interbank exposure limits and pandemic restrictions. This threshold reflects consistent patterns across domains and underscores the need for regulatory mechanisms that balance connectivity's benefits with contagion risks[38,39]. More than a model artifact, this threshold represents a phase transition in cascade dynamics, analogous to percolation transitions in physical systems. Below it, networks cannot sustain global cascades; above it, giant components enable system-wide failures. Real-world systems often self-organize near this critical region, highlighting the need for coordinated schemes that preserve beneficial interconnectedness while limiting rapid contagion.

Fourth, based on our simulation results, the model suggests a centrality-based heuristic in which each agent selects a protection level that evolves through social learning and strategy exploration. These points reflect dual-process theory, which posits that decision-making draws on both intuitive (heuristic) and analytical processes[40]. This aligns with Kahneman's observations that biased intuitive judgments can lead to suboptimal outcomes[41]. In our simulations, comparing protective success with and without the centrality-based heuristic illustrates the complex dynamics of decision-making under crisis conditions, underscoring the importance of understanding how heuristic strategies guide protective behavior in uncertain environments. Previous research supports this view, highlighting the value of behavioral principles in shaping investment decisions during instability[42] and emphasizing the need to recognize and counter biases in intervention strategies—a theme echoed in our findings. Moreover, our results show that the protective strategy f_{p} can be highly sensitive to stochastic effects (σ_{e}), mirroring real-world uncertainties, yet certain components (particularly f_{p1}, linked to network centrality) remain comparatively robust at moderate noise levels (up to $\sigma_{\mathrm{e}} = 0.1$). In contrast, f_{p0}, lacking direct engagement through centrality, exhibits more pronounced variability, underscoring how heuristic-driven decisions may diverge sharply as σ_{e} increases and demonstrating the model's ability to capture realistic, noise-driven instabilities in agent behavior[40,42].

Finally, building on these mechanisms, our analysis shows that centrality's influence on investment persists over time, driving convergence toward stable but differentiated protection levels. High-centrality nodes act as firewalls, investing heavily in protective measures, while peripheral nodes allocate fewer resources [43]. This produces a steady-state equilibrium in which each node's strategy reflects its connectivity, though this outcome may not be collectively optimal. Our findings suggest that collaborative agreements and regulatory oversight can enhance resilience by aligning individual incentives with systemic stability.[44]

Several limitations guide interpretation. The memorized capital mechanism [$c_m = m_e * c_{new} + (1 - m_e) * c_{old}$] captures short-term adaptation, whereas longer memory horizons, as shown in multi-agent studies[45], could alter protection dynamics. Temporal interaction frequency highlighted in recent network research[46], may also modulate contagion speed. Although our model assumes daily synchronous interactions, real networks operate on heterogeneous timescales that may create temporal firewalls limiting cascades. Compared with similar centrality-based protection studies[47], our saturating protection function and memorized capital dynamics produce distinct equilibria, including protection plateaus that prevent over-investment by central nodes. The single protection variable f_{p} simplifies real instruments such as capital, liquidity, or derivatives. All nodes follow identical behavioral rules despite real systems comprising diverse agent types. Agents imitate successful strategies but do not learn optimal responses or anticipate others' actions strategically. Parameters such as p_{n}, p_{l}, and σ_{e} require empirical grounding beyond our sensitivity analysis[15,37]. Despite these limitations, the model shows how local optimization can generate globally suboptimal outcomes, offering a game-theoretic perspective on interventions that shift networks toward more resilient[29], higher-investment regimes.

Consequently, our research offers new perspectives on how risk and failure propagate in networked systems, emphasizing the value of leveraging high-quality connections for effective risk sharing[48]. Public health officials can design gathering restrictions that balance social needs with contagion risk, and sports leagues can structure competitions to maintain competitive balance without tactical monotone[49]. The centrality-based protection heuristic provides a unified core for guiding protective investment decisions. These insights inform contagion management and support robust systemic risk strategies. Focusing on node centrality, protective investment, and strategic cooperation mechanisms[44] highlights essential elements for strengthening network resilience.

Methods

The simulation captures how network topology, individual decision-making, and systemic risk interact. We construct the network algorithm and initialize heterogeneous agents with different capital endowments, protection strategies, and positions. The dynamic phase unfolds in iterative timesteps, each comprising four sequential processes: failure propagation via shocks and contagion, protection-mediated resolution, capital updates with memory effects, and strategy evolution through social learning and exploration (Fig. 7, upper left panel). This approach adopts deliberate simplifications to highlight key mechanisms (see Appendix 8 for the pseudocode): binary failure states aligned with regulatory and empirical thresholds, a saturating protection function reflecting diminishing returns, and a static network topology to separate behavioral from structural effects. These abstractions allow tractable analysis while preserving essential risk dynamics (Fig. 7, upper right panel). Subsequent subsections outline each component, with mathematical formulations and parameters provided where relevant.

Network Properties: Our study is based on a scale-free network designed for structural comparisons (Fig. 2), using a custom algorithm referencing the Barabási–Albert model to depict interconnected systems prone to systemic risk. We used the (n, m, $seed$) function to generate a graph with preferential attachments. The notation is as follows: n = the total number of nodes in the graph, m = the number of edges attached from a new node to existing nodes, and $seed$ = a seed for the random number generator for reproducibility (see Appendix 9's Table S4 for the details). The graph employs "preferential attachment," meaning that the more connected a node is, the more likely it is to receive new links. Nodes are added individually, and each new node connects to m existing nodes with a probability proportional to their degree. The function begins with an initial network of m nodes. For each new node, a probability is computed for each existing node i using

$$p(i) = k_{\mathrm{i}} \,/\, k$$

where $p(i)$ is the probability of connecting to node i, k_{i} is the degree of node i (the number of connections node i has to other nodes), and k is the sum of all node degrees. The new node is then connected to m existing nodes according to these probabilities, and the procedure continues until n nodes populate the graph. We selected this function for its simplicity,

reliability in scientific research, computational efficiency, and reproducibility via a fixed random seed. Because our study does not require additional flexibility, this approach provides a clear and consistent method for generating scale-free networks. This feature highlights their ubiquity and resilience, governed by the rule:

$$p_i = k_i \,/\, \sum_i p_i$$

Here, k_i is the degree of node *i*, and the sum extends over all nodes *j*. The network begins with a connected array of m_0 nodes. Each new node attaches to $m < m_0$ existing nodes with probability proportional to their link count. The resulting degree distribution follows

$$p(k) \sim k^{-\gamma}$$

where k is a node's degree, and γ denotes the degree exponent. For many real-world networks, this value typically ranges between 2 and 3. In our model, the network comprises n nodes or agents, representing the finite number of participants in systems exposed to systemic risk. These nodes are interconnected through preferential attachment, a defining feature of scale-free networks in which highly connected nodes are more likely to attract new links. This structure is represented by an adjacency matrix A, which records the connections between nodes.

$$a_{i,j} = \begin{cases} 1 & if\ \{i,j\} \in E \\ 0 & otherwise \end{cases} \quad \rightarrow \quad A(m,n) = \begin{array}{c} \\ 1 \\ 2 \\ 3 \\ 4 \end{array} \begin{array}{c} \begin{array}{cccc} 1 & 2 & 3 & 4 \end{array} \\ \begin{bmatrix} 0 & 1 & 0 & 0 \\ 1 & 0 & 1 & 1 \\ 0 & 1 & 0 & 1 \\ 0 & 1 & 1 & 0 \end{bmatrix} \end{array} \quad \rightarrow \quad \begin{array}{l} \deg(v_{2m}) = 3 \\ \\ \deg(v_{2n}) = 3 \end{array}$$

In the schematic adjacency matrix $a_{i,j}$, whose entries derive from $A(m,n)$, the node (or vertex) 2 has three connections $[\deg(v_{2m}) = 3, \deg(v_{2n}) = 3]$.

Network Size: We primarily use $n = 100$, $m = 10$ for core analyses. Optimal connectivity emerges from balancing protection costs against cascade risks. Following percolation theory for scale-free networks, the critical threshold for global cascades is $k_c = k/k^2/k - 1$, where k is the average degree and k^2 is the second moment of the degree distribution. Protection cost scales as $C_p \propto kf_p$, while cascade damage scales as $D \propto k^2 P(cascade)$, where $P(cascade)$ is the probability of system-wide failure. Optimal connectivity k^* minimizes total expected loss: $L(k) = C_p(k) + P(failure)D(k)$. Taking the derivative and setting $dL/dk = 0$ yields $k^* \approx \sqrt{C_p/D}$, where C_p and D are the derivatives of the cost and damage functions. For our parameter values, this gives $k^* \approx 0.1n$, corresponding to 10% connectivity (empirically demonstrated in Fig. 3.1). Scaling to more nodes or connections to strengthen the system during evolutionary dynamics also alters network behavior in several ways: (i) in larger networks, eigenvector centrality values become more dispersed, influencing heuristic calibration; (ii) full simulations involving many nodes and long timesteps (i.e., t = 3,000,000, r = 10) require substantial computational resources; and (iii) the saturating protection function parameters need recalibration for different network sizes (parameter sensitivity; see S12 in Appendix 5.2). To address scalability concerns, we validated the model across multiple networks with comparative analyses (Fig. 4.1, 4.2, 5, 6.2). Although quantitative thresholds shift, the qualitative link between centrality and optimal protection remains consistent. Building on these mechanisms, we structured the analysis around principles involving network and agent properties, failure and payoff dynamics, and strategy evolution.

Failure Dynamics: The model captures the binary nature of systemic risk, with each agent transitioning between two states: "not failed" or "failed." All agents begin in the "not failed" state, highlighting how a single transition may precipitate broader systemic failure. At each timestep, a node may fail spontaneously with probability p_n. This failure potential can spread along each link with probability p_l, underscoring the contagion process inherent in systemic risk.

Failure propagation was simulated through iterative processes in which nodes may fail due to initial conditions (p_n) or through spread from connected nodes (p_l). This dual mechanism reflects the complexity of real-world systemic risks, from bank failures causing financial contagion, to patient-zero events in epidemics, to injuries cascading through sports teams, capturing both random initial shocks and structured network-driven transmission (see Appendix 9, Table S5 for details).

The failure potential becomes an actual failure with probability $1 - p_p$, r reflecting how mitigation efforts reduce failure likelihood. We calculate p_p using

$$p_p = p_{p,max}/(1 + c_{p,1/2}/(f_p c))$$

This formulation incorporates an agent's capital c, the fraction f_p invested in protection, the maximum protection level $p_{p,max}$, and the half-maximal effective concentration $c_{p,1/2}$, highlighting the relationship between individual risk behaviors and systemic propagation (see Appendix 9, Table S6 for the details). Conceptually, this represents the effectiveness of an agent's protection strategy. The protective effect increases as invested capital ($f_p c$) rises, but the benefit diminishes once investment nears or exceeds $c_{p,1/2}$. The parameter $c_{p,1/2}$ therefore denotes the threshold at which protection effectiveness reaches 50% of its maximum, a value with concrete empirical interpretations across domains (see Supplementary Appendix 10 for more detail).

Investing additional capital in protection eventually yields diminishing returns in reducing failure probability. This reflects a saturation effect: beyond a certain point, adding resources does not proportionally improve protection. Thus, agents cannot eliminate failure risk simply by overspending; instead, they must balance investing enough to meaningfully reduce risk without wasting capital on negligible gains. This dynamic is central to our model's analysis of systemic risk mitigation.

Protection Function Derivation: Our protection function derives from first principles of risk management. Consider an agent investing fraction f_p of capital c in protection. The protection effectiveness must satisfy three constraints: (i) zero investment yields zero protection $p_p(0) = 0$, (ii) protection saturates at maximum $\lim_{f_p c \to \infty} p_p = p_{p,max}$, (iii) diminishing marginal returns $\frac{d^2 p_p}{d(f_p c)^2} < 0$. These constraints, together with cost-benefit optimization, where agents maximize expected utility $U = (1 - p_{failure}) c_{remaining} - f_p c$, yield the first-order condition $\frac{dU}{df_p} = p_p(f_p c) c \times c_{remaining} - c = 0$. Solving for the optimal protection function that satisfies all constraints produces the hyperbolic form [$p_p = p_{p,max}/(1 + c_{p,1/2}/(f_p c))$]. This form arises naturally from empirical optimization principles analogous to resource allocation under diminishing returns (see Appendix 11, for more detail).

Payoff Dynamics: The payoff dynamics assume each agent receives a unit payoff at every timestep. This is added to capital c, which is then allocated to maintenance (f_m) and protection (f_p), yielding updated capital (see Appendix 9, Table S7 for the details):

$$c_{new} = 1 + (1 - f_m - f_p) c$$

Reflecting recent findings on memory effects, we incorporated a stochastic moving average [MA(1)] mechanism into the dynamics; $x_n = \varepsilon_n + b_1 \varepsilon_{n-1}$. Each agent retains a "memory" of its capital, described by

$$c_m = m_e * c_{new} + (1 - m_e) * c_{old}$$

Here, m_e represents memory strength, weighting current capital (c_{new}) against the remembered capital (c_{old} and thereby modeling the agent's perception of its state (see Appendix 9, Table S8 for the details).

Our memorized capital mechanism represents a significant departure from traditional evolutionary game approaches, which often assume myopic best-response dynamics or instantaneous fitness comparisons. By incorporating the stochastic moving average c_m, we capture three features absent in standard models: (i) time-horizon effects through weighted historical performance, (ii) information processing through exponential decay (memory parameter m_e), and (iii) strategy assessment via a smoothed success trajectory. This innovation reflects empirical evidence that institutions evaluate strategies based on sustained performance rather than instantaneous outcomes, banks assess capital policies across business cycles, hospitals evaluate protocols across cohorts, and sports teams measure prevention effectiveness over seasons. The memory parameter m_e thereby captures institutional inertia: lower values (persistent memory) characterize conservative sectors like banking, whereas higher values (adaptive memory) suit dynamic environments such as pandemic response (see Appendix 3 for the details).

Strategy Dynamics. In interconnected networks, each agent develops a strategy to manage capital and reduce failure risk. The primary variable is the protection level, f_{p}, which agents adjust to lower systemic vulnerability. Each agent determines its protection level through the heuristic:

$$f_{\mathrm{p}} = f_{\mathrm{p0}} + f_{\mathrm{p1}} C$$

This heuristic is truncated to the interval $(0, 1 - f_{\mathrm{m}})$, ensuring that the sum of the protection and maintenance fractions (f_{p0} and f_{p1}) does not exceed 1, reflecting each agent's limited resources. In this heuristic, f_{p0} represents a baseline protection level maintained regardless of network position, whereas f_{p1} adjusts protection in response to an agent's centrality. The centrality term C is normalized to (0,1), indicating that more central agents invest more in protection. The strategy values f_{p0} and f_{p1} evolve through two mechanisms: social learning and strategy exploration. In social learning, at each timestep, an agent with probability p_{r} selects another agent as a role model and imitates that agent's strategy values with probability p_{i} (see Appendix Table S9 for the details):

$$p_{\mathrm{i}} = 1/(1 + \exp(-s\Delta c))$$

Here, s denotes selection strength, and Δc is the difference between the role model's memorized capital and the focal agent's memorized capital. A larger Δc value indicates greater accumulated success, increasing the likelihood of imitation. This Fermi-based learning rule is empirically observed across domains such as banking, epidemiology, and sports (Appendix 11). Strategy exploration reflects agents' tendency toward experimentation: at each timestep, with probability p_{e} an agent randomly selects one of its two strategy values (f_{p0} and f_{p1}) and modifies it by a normally distributed increment with mean 0 and standard deviation σ_{e} (see Table S10 in Appendix 9).

We selected the Fermi update rule for strategy imitation based on bounded rationality theory in institutional decision-making[40,50]. Unlike perfectly rational agents, real-world decision-makers such as bank executives, public health officials, or team managers operate with cognitive limits and incomplete information. Utility maximization under uncertainty is expressed as $U_{\mathrm{i(adopt)}} - U_{\mathrm{i(keep)}} = \beta[\pi_{\mathrm{j}} - \pi_{\mathrm{i}}] + \varepsilon$. where β reflects sensitivity to performance differences, π denotes observed payoffs, and ε represents decision noise. Under logit choice assumptions, this yields the Fermi probability $p_{\mathrm{i}} = 1/(1 + \exp(-s\Delta c))$, where $s = \beta/\sigma_{\varepsilon}$ represents the signal-to-noise ratio in institutional decision-making. Empirical studies in organizational learning support this formulation[51], which captures the S-shaped adoption curves observed in innovation diffusion. The selection-strength parameter s reflects "institutional confidence," the precision with which organizations assess and adopt successful strategies: (i) $s < 1$ (low confidence high-uncertainty environments with noisy performance signals (e.g., emerging markets, novel pathogens); (ii) $s = 1$ (moderate confidence): balanced assessments

typical of mature systems (e.g., established banking sectors, endemic disease management); (iii) $s > 1$ (high confidence): clearer performance indicators with lower ambiguity (e.g., regulated markets, standardized sports leagues).

This alteration reflects that agents may adjust their strategies through random exploration or in response to changing environmental conditions. The interaction of these mechanisms enables our model to examine how agents' behaviors and strategic choices influence systemic risk propagation in interconnected networks.

Model Initialization and Iteration: The simulation begins by randomly assigning agents to network nodes, each initialized with capital (c) and strategy values (f_{p0} and f_{p1}). Initial capital is drawn from a uniform distribution ranging from 0 to 1, and strategy values are drawn from a normal distribution with a specified mean and standard deviation. These values are then constrained to the interval (0,1). The model proceeds through discrete time steps in which agents update their capital based on current capital, maintenance investment (f_{m}), and the shock experienced. Simultaneously, agents adjust their protection strategy (f_{p}) through social learning and strategy exploration, as described in the Strategy Dynamics section. Iteration across time steps reveals how network structure, protection strategies, and initial conditions shape systemic risk. The coupled dynamics of risk propagation, capital growth, and strategy adaptation show how agent behavior contributes to network resilience or vulnerability (see Appendices 7–9 for details).

References

1. Benston, G. J. & Kaufman, G. G. Is the banking and payments system fragile? *J. Financ. Serv. Res.* **9,** 209–240 (1995). https://doi.org/10.1007/BF01051747.
2. Battiston, S., Delli Gatti, D., Gallegati, M., Greenwald, B. & Stiglitz, J. E. Default cascades: when does risk diversification increase stability? *J. Financ. Stab.* **8,** 138–149 (2012). https://doi.org/10.1016/j.jfs.2012.01.002.
3. Allen, F. & Gale, D. Financial contagion. *J. Polit. Econ.* **108,** 1–33 (2000). https://doi.org/10.1086/262109.
4. Haldane, A. G. & May, R. M. Systemic risk in banking ecosystems. *Nature* **469,** 351–355 (2011). https://doi.org/10.1038/nature09659.
5. Gai, P., Haldane, A. & Kapadia, S. Complexity, concentration and contagion. *J. Monet. Econ.* **58,** 453–470 (2011). https://doi.org/10.1016/j.jmoneco.2011.05.005.
6. May, R. M., Levin, S. A. & Sugihara, G. Complex systems: ecology for bankers. *Nature* **451,** 893–894 (2008). https://doi.org/10.1038/451893a.
7. Thurner, S. & Poledna, S. DebtRank-transparency: controlling systemic risk in financial networks. *Sci. Rep.* **3,** 1888 (2013). https://doi.org/10.1038/srep01888.
8. Albert, R. & Barabási, A.-L. Statistical mechanics of complex networks. *Rev. Mod. Phys.* **74,** 47–97 (2002). https://doi.org/10.1103/RevModPhys.74.47.

9. Joseph, D. L. & Newman, D. A. Emotional intelligence: an integrative meta-analysis and cascading model. *J. Appl. Psychol.* **95,** 54–78 (2010). https://doi.org/10.1037/a0017286.

10. Yeoh, P. Causes of the global financial crisis: learning from the competing insights. *Int. J. Disclosure Gov.* **7,** 42–69 (2010).

11. Kapata, N. *et al.* Is Africa prepared for tackling the COVID-19 (SARS-CoV-2) epidemic? Lessons from past outbreaks, ongoing Pan-African public health efforts, and implications for the future. *Int. J. Infect. Dis.* **93,** 233–236 (2020). https://doi.org/10.1016/j.ijid.2020.02.049.

12. Park, C. Role of recovery in evolving protection against systemic risk: a mechanical perspective in network-agent dynamics. *Complexity* **2021,** 4805404 (2021). https://doi.org/10.1155/2021/4805404.

13. Buldyrev, S. V., Parshani, R., Paul, G., Stanley, H. E. & Havlin, S. Catastrophic cascade of failures in interdependent networks. *Nature* **464,** 1025–1028 (2010). https://doi.org/10.1038/nature08932.

14. Strogatz, S. H. Exploring complex networks. *Nature* **410,** 268–276 (2001). https://doi.org/10.1038/35065725.

15. Su, Q., McAvoy, A. & Plotkin, J. B. Strategy evolution on dynamic networks. *Nat. Comput. Sci.* **3,** 763–776 (2023). https://doi.org/10.1038/s43588-023-00509-z.

16. Brummitt, C. D., D'Souza, R. M. & Leicht, E. A. Suppressing cascades of load in interdependent networks. *Proc. Natl Acad. Sci. USA* **109,** E680–E689 (2012). https://doi.org/10.1073/pnas.1110586109.

17. Barabási, A.-L. Scale-free networks: a decade and beyond. *Science* **325,** 412–413 (2009). https://doi.org/10.1126/science.1173299.

18. Haldane, A. Why banks failed the stress test. *BIS Rev.* **18,** (2009).

19. Haldane, A. Small lessons from a big crisis. In *Remarks at the Federal Reserve Bank of Chicago 45th Annual Conference: Reforming Financial Regulation* 8 (2009).

20. Jamali, M. & Ester, M. A matrix factorization technique with trust propagation for recommendation in social networks. In *Proceedings of the Fourth ACM Conference on Recommender Systems* 135–142 (2010).

21. Gai, P. & Kapadia, S. Contagion in financial networks. *Proc. R. Soc. A* **466,** 2401–2423 (2010). https://doi.org/10.1098/rspa.2009.0410.

22. Cohen, L. E., Fagre, A. C., Chen, B., Carlson, C. J. & Becker, D. J. Coronavirus sampling and surveillance in bats from 1996–2019: a systematic review and meta-analysis. *Nat. Microbiol.* **8,** 1176–1186 (2023). https://doi.org/10.1038/s41564-023-01375-1.

23. Bonacich, P. Some unique properties of eigenvector centrality. *Soc. Netw.* **29,** 555–564 (2007). https://doi.org/10.1016/j.socnet.2007.04.002.

24. Barabási, A.-L. & Bonabeau, E. Scale-free networks. *Sci. Am.* **288,** 60–69 (2003). https://doi.org/10.1038/scientificamerican0503-60.

25. Bonacich, P. Factoring and weighting approaches to status scores and clique identification. *J. Math. Sociol.* **2,** 113–120 (1972). https://doi.org/10.1080/0022250X.1972.9989806.

26. Park, C. Network and agent dynamics with evolving protection against systemic risk. *Complexity* **2020,** 2989242 (2020). https://doi.org/10.1155/2020/2989242.

27. Samuelson, W. & Zeckhauser, R. Status quo bias in decision making. *J. Risk Uncertain.* **1,** 7–59 (1988). https://doi.org/10.1007/BF00055564.

28. Dawes, R. M. Social dilemmas. *Annu. Rev. Psychol.* **31,** 169–193 (1980). https://doi.org/10.1146/annurev.ps.31.020180.001125.

29. Olson, M. *The Logic of Collective Action: Public Goods and the Theory of Groups* (Harvard Univ. Press, 1971).

30. Axelrod, R. *The Evolution of Cooperation* (Basic Books, 1984).

31. Pozzi, F., Di Matteo, T. & Aste, T. Spread of risk across financial markets: better to invest in the peripheries. *Sci. Rep.* **3,** 1665 (2013). https://doi.org/10.1038/srep01665.

32. Ostrom, E. *Governing the Commons: The Evolution of Institutions for Collective Action* (Cambridge Univ. Press, 1990).

33. Yamagishi, T. The provision of a sanctioning system as a public good. *J. Pers. Soc. Psychol.* **51,** 110–116 (1986). https://doi.org/10.1037/0022-3514.51.1.110.

34. Vinogradov, E., Leick, B. & Kivedal, B. K. An agent-based modelling approach to housing market regulations and Airbnb-induced tourism. *Tour. Manag.* **77,** 104004 (2020). https://doi.org/10.1016/j.tourman.2019.104004.

35. Taylor, S. *Health in a Post-COVID World: Lessons from the Crisis of Western Liberalism* (Policy Press, 2023).

36. Friedberg, A. *Through a Screen Darkly: Psychoanalytic Reflections During the Pandemic* (Routledge, 2021).

37. Dziubiński, M. & Goyal, S. Network design and defence. *Games Econ. Behav.* **79,** 30–43 (2013). https://doi.org/10.1016/j.geb.2012.12.007.

38. Park, C. Potential consequence of interconnected intervention against systemic risk (COVID-19) via a model-driven network-agent dynamic. *Complexity* **2022,** 7382033 (2022). https://doi.org/10.1155/2022/7382033.

39. Hipsey, M. R. *et al.* Predicting the resilience and recovery of aquatic systems: a framework for model evolution within environmental observatories. *Water Resour. Res.* **51,** 7023–7043 (2015). https://doi.org/10.1002/2015WR017175.

40. Kahneman, D. *Thinking, Fast and Slow* (Macmillan, 2011).

41. Kruglanski, A. W. & Gigerenzer, G. Intuitive and deliberate judgments are based on common principles. *Psychol. Rev.* **118,** 97–109 (2011). https://doi.org/10.1037/a0020762.

42. Bachmann, K. & Hens, T. Behavioral finance and investment advice. In *Handbook of Behavioral Finance* (Edward Elgar, 2010).

43. Acemoglu, D., Ozdaglar, A. & Tahbaz-Salehi, A. Systemic risk and stability in financial networks. *Am. Econ. Rev.* **105,** 564–608 (2015).

44. Goyal, S. *Connections: An Introduction to the Economics of Networks* (Princeton Univ. Press, 2007).

45. Ren, T. & Zeng, X. J. Enhancing cooperation through selective interaction and long-term experiences in multi-agent reinforcement learning. *arXiv* preprint arXiv:2405.02654 (2024).

46. He, Y. *et al.* Temporal interaction and its role in the evolution of cooperation. *Phys. Rev. E* **110,** 024210 (2024). https://doi.org/10.1103/PhysRevE.110.024210.

47. Ren, T. & Zeng, X. J. Reputation-based interaction promotes cooperation with reinforcement learning. *IEEE Trans. Evol. Comput.* **28,** 1177–1188 (2023). https://doi.org/10.1109/TEVC.2023.3304911.

48. Newman, M. *Networks* (Oxford Univ. Press, 2018).

49. Park, C. Optimizing resilience in sports science through an integrated random network structure: harnessing the power of failure, payoff and social dynamics. *SAGE Open* **15,** 21582440251316513 (2025).

50. Simon, H. A. *Models of Man: Social and Rational* (John Wiley & Sons, 1957).

51. Argote, L. & Miron-Spektor, E. Organizational learning: from experience to knowledge. *Organ. Sci.* **22,** 1123–1137 (2011). https://doi.org/10.1287/orsc.1100.0596.

Acknowledgments

Data Availability Statement

All data generated or analysed during this study are included in this article [and its supplementary information files].

Funding

This work was supported by the Basic Science Research Program through the National Research Foundation of Korea (NRF), funded by the Ministry of Education (Grant Number: 2020R1l1A1A01056967). Additional support was provided by the Seoul National University BK21 Four Program.

Ethics Statement

Use of AI

Competing Interests

Author Contributions

Figure legends

Figure 1. Protection dynamics in scale-free networks under different scenarios. The left panel (A) illustrates sufficient protection with adequate capital (cyan), where protected nodes (blue) resist a failure cascade despite initial failures. The right panel (C) shows insufficient protection leading to system-wide failure (red nodes). Network visualization uses node color (blue = protected, red = failed) and size (proportional to degree) to depict state evolution (the upper portion of panel B). The phase diagram identifies critical protection thresholds for preventing cascading failures (the lower portion of panel B); it presents the phase space of protection strength versus failure probability, showing how the equilibrium point (white circle) shifts between safe (blue) and failed (red) regions.

Figure 2. Conceptual comparison of failure across different networks. The upper plots illustrate structural properties of each network type and highlight vulnerability patterns under varying connectivity and failure probabilities. The bottom plots show the relationship between normalized failure probabilities (x-axis) and transformed failure probabilities (y-axis). Color intensity reflects failure-rate density, and error bars represent interquartile ranges across simulations. Note: they depict variations in failure outcomes as functions of initial failure probabilities p_{n} and p_{l}, across several network topologies (number of nodes = 100).

Figure 3.1. Simulation results for selected connectivity levels across network topologies. Failure probability (red circles) and memorized capital (blue circles) are plotted as functions of connectivity for random (Erdős–Rényi), regular, small-world (Watts–Strogatz), and scale-free (Barabási–Albert) networks. All topologies display a critical transition near 10% connectivity (vertical gray line), after which failure probability plateaus and memorized capital stabilizes near unity. Simulation parameters: number of nodes = 100; number of connections per node = 1–99, $p_{\max}$= 1, $c_{\mathrm{p},1/2}$ = 0.05, initial failure p_{n} = 0.1, p_{l} = 0.3, initial capital c = 1, maintenance f_{m} = 0.1, time steps = 1–100,000 (periods 1–100,000), realization = 1 (see Appendix 2 for more details). Error bars represent standard deviation over time.

Figure 3.2. Combined simulation results for memorized capital under varying imitation and exploration levels (0.0–0.9). The left panel uses the following parameters: type of network = scale free (Barabási–Albert model), number of nodes = 100, number of connections per node = 10, p_{max} = 1, $c_{p,1/2}$ = 0.05, initial failure p_n = 0.1, p_l = 0.3, initial capital c = 1, maintenance f_m = 0.1, strength of selection, s = 1, σ_e = 0.001, and time steps = 10,000. Observations from grids with differing spacings (0.001–0.009; 0.01–0.09; 0.1–0.9) are combined into one panel. The right panel shows network property results focused on imitation (pr = 0.1–0.9) when exploration is low, pe = 0.1 (left portion), and exploration is high, pe = 0.9 (right portion). Type of network = scale free (Barabási–Albert model), number of nodes = 500, number of connections per node = 10, p_{max} = 1, $c_{p,1/2}$ = 0.05, initial failure p_n = 0.1, p_l = 0.3, initial capital c = 1, maintenance f_m = 0.1, strength of selection, s = 1, σ_e = 0.001, time steps = 100,000, realization = 1.

Figure 4.1. Representation of network properties and simulation results. Upper panel: The left portion shows the average value (me_ca = memorized capital, failure) across expected degree (m = 1–99: horizontal axis), illustrating why m = 10 is used in simulations. The right portion displays the scale-free network type (Barabási–Albert model) and its preferential attachment features; number of nodes = 100; number of connections per node = 10. Bottom panel: Simulation results for memorized capital with imitation (p_r = 0.1) values. Initialized parameters: network type = scale-free, number of nodes = 100, number of connections per node = 10, p_{max}= 1, $c_{p,1/2}$ = 0.05, initial failure p_n = 0.1, p_l = 0.3, initial capital c = 1, maintenance f_m = 0.1, strength of selection, s = 1, σ_e = 0.001, time steps = 50,000. Right portion: average value (me_ca = memorized capital, failure) according to the expected degree (m = 1–99: horizontal axis). See Appendix 5 for results using expanded and alternative parameter combinations; expanded results with time steps = 10,000, and alternative results with exploration (p_{e} = 0.9), imitation (p_{r} = 0.1); exploration (p_{e} = 0.9), imitation (p_{r} = 0.9).

Figure 4.2. Comparative analysis of protection heuristics and empirical validation. Upper left: temporal evolution of failure rates comparing centrality-based protection with random and uniform allocation strategies. Upper center: scatter plot showing the correlation between eigenvector centrality and protection investment (R^2). Upper right comparison of centrality metrics showing eigenvector centrality outperforms degree, betweenness, and closeness. Bottom left: heatmap of network performance as a function of nodes (n) and connections (m), with R^2 values indicating predictive accuracy. Bottom right: multi-domain empirical validation of 10% optimal connectivity. All domains show performance peaks at 9–12% connectivity (mean: 10.3%, standard deviation: 1.2%). The theoretical model (gray curve) aligns with empirical patterns, and the shaded region denotes the optimal (8–12%) zone. See Appendix 5.2 for detailed methodology and data sources.

Figure 5. Selected individual results referenced by Fig. 4.1. Upper panel initialized parameters: network type = scale-free (Barabási–Albert), number of nodes = 1000, number of connections per node = 100, $p_{\max}$= 1, $c_{\mathrm{p},1/2}$= 0.05, initial failure p_{n} = 0.1, p_{l} = 0.3, initial capital c= 1, maintenance f_{m} = 0.1, strength of selection, s= 1, σ_{e} = 0.0001, time steps = 30,000, realization = 10 (left portion), time steps = 300,000, realization = 5 (right portion). The lower panel presents results for a smaller network with number of nodes = 100, number of connections per node = 10, $p_{\max}$= 1, $c_{\mathrm{p},1/2}$= 0.05, initial failure p_{n} = 0.1, p_{l} = 0.3, initial capital c= 1, maintenance f_{m} = 0.1, strength of selection, s= 1, σ_{e} = 0.0001, time steps = 3,000,000, realization = 1. The right portion shows investment values (vertical

axis) at t =3,000,000 according to the eigenvector_centrality (horizontal axis) value (color bar) for each strategy value (right), and its regression (see legend: calculated R-squared for f_{p} , f_{p0}, and f_{p1}).

Figure 6.1. Comparative phase portraits illustrating the effects of different stochastic influences. The left plot shows the phase portrait under low noise (σ = 0.001), where the system exhibits a stable, synchronized relationship between f_{p} values, converging toward a stable attractor (marked by a yellow density circle). Scatter markers represent protection investment (f_{p}), with colors indicating intensity (low: blue, high: red), while arrows show the convergence direction. The middle and right plots represent increased noise levels (σ_{e} = 0.01 and σ_{e} = 0.1, respectively), illustrating how greater stochastic influences introduce variability and anti-synchronized dynamics.

Figure 6.2. Comparative diagrams illustrating how distinct stochastic influences (σ_{e}) shape final outcomes in the (f_{p0} and f_{p1}) planes. The horizontal axis shows six noise levels ($\sigma_{\mathrm{e}} \in \{0.0001, 0.001, 0.01, 0.1, 0.5, 0.9\}$), and the circles represent each noise level's average attractor (f_{p0} and f_{p1}). The color map depicts the kernel density of aggregated outcomes, and the center arrows indicate local directions of strategy shifts around a midpoint. Notably, two overlapping vertical diagrams (with flow lines in f_{p0}, f_{p1}-space) highlight stable versus unstable behaviors: At σ_{e} = left vertical line, arrows converge toward a stable fixed point in f_{p1}. At an artificial σ_{e} = drawn to the far right, arrows diverge, illustrating an unstable reference point. Note: for the simulation shown in the top panel, number of nodes = 100, connection probability = 0.1%, time period = 10,000, realization = 10; for the simulation in the bottom panels, number of nodes = 100 (left) and 1000 (right), connection probability = 0.1%, time period = 10,000, realization = 10 (showing similar trends despite minor sensitivity differences due to variation in nodes and connections).

Figure 7. Mechanical rationalization for protection–failure and social dynamics. The upper-left plot presents a simplified sequential workflow, and the right plot shows its mechanism in detail as a flowchart. Boxes depict key state variables (e.g., c for capital, m_c for memorized capital) and strategic elements (f_{p} for the protection fraction), whereas ellipses denote parameters such as p_{n}, p_{l}, and p_{e}. Solid arrows illustrate direct influences, e.g., capital updates, failure transitions, and social learning pathways, while dashed arrows highlight auxiliary effects, including memory weighting and maintenance costs. Empirically, the lower panels show how simulated agents explore the parameter space and converge toward characteristic regimes, capturing the interplay between protection strategies, failure rates, and social adaptation within the model workflow. Colored flow lines in blue represent a system with high protection and minimal failure propagation. By contrast, the rightmost panel shows flow lines in red, reflecting a highly vulnerable system with strong failure propagation and low maximum protection. Intermediate panels illustrate a gradual transition driven by investment (f_p) embedded in its strategic (f_{p0} and f_{p1}) centrality (C) between these extremes (three sets of trajectories are overlaid on the data).

Figure 8. Empirical calibration and cross-domain validation of the centrality-based protection framework. Left panel: Protection effectiveness versus normalized investment reveals domain-specific saturation dynamics following the hyperbolic function $p_{\mathrm{p}} = p_{\mathrm{p,max}}/(1 + c_{\mathrm{p},1/2}/(f_{\mathrm{p}}c))$, with fitted half-saturation constants ($c_{\mathrm{p},1/2}$) for banking, epidemiology, and sports, all demonstrating strong fits (R^2). Right panel: Social learning dynamics show consistent Fermi-type adoption patterns $p_{\mathrm{i}} = 1/(1 + \exp(-s\Delta c))$ across domains, with selection strengths s = 0.9–1.1, indicating universal behavioral responses to performance differentials (regions reflect domain-specific learning neighborhoods). Middle panel: A three-dimensional validation surface confirms robust predictive power, with strong correlations between model predictions and empirical outcomes (banking, epidemiology, sports mean r = 0.694; See Appendix 10 and 11 for details and data sources).

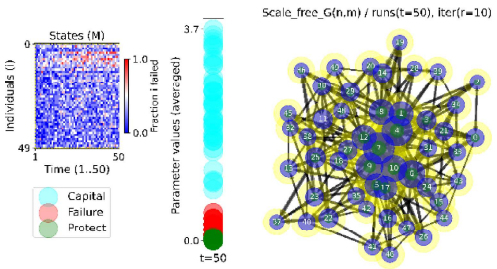

(A) Scenario = sufficient protection

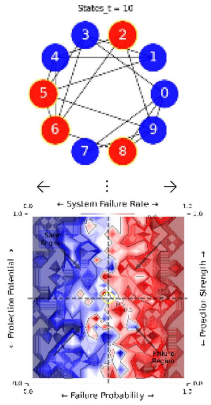

(B) Phase space

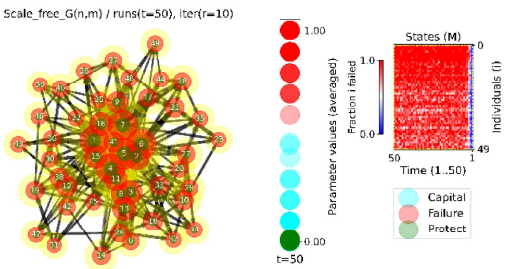

(C) Scenario = insufficient protection

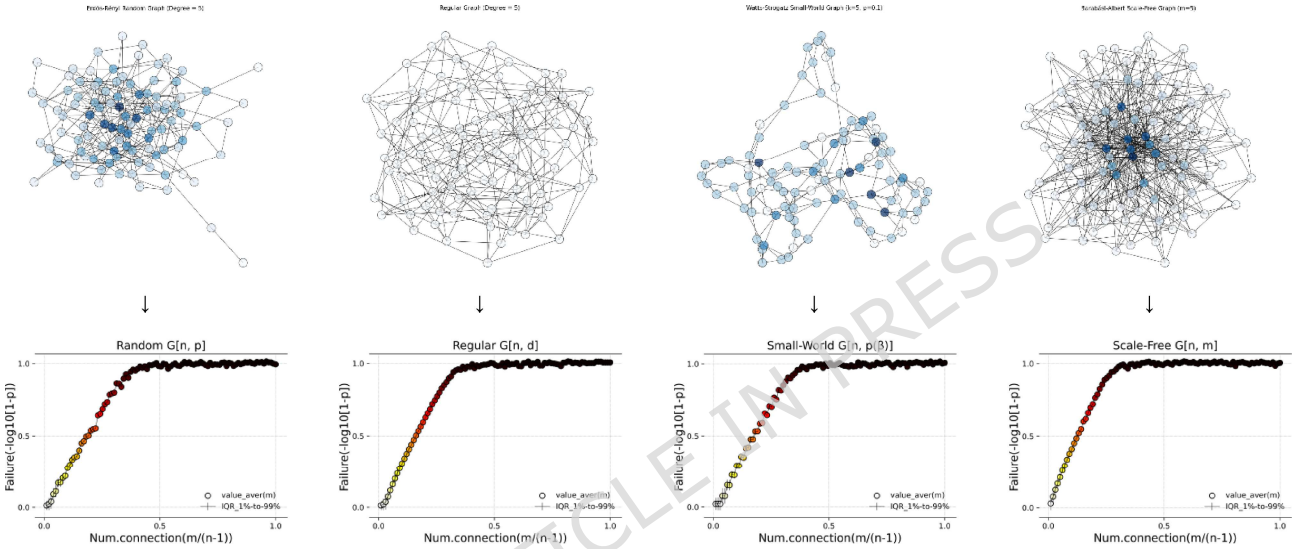

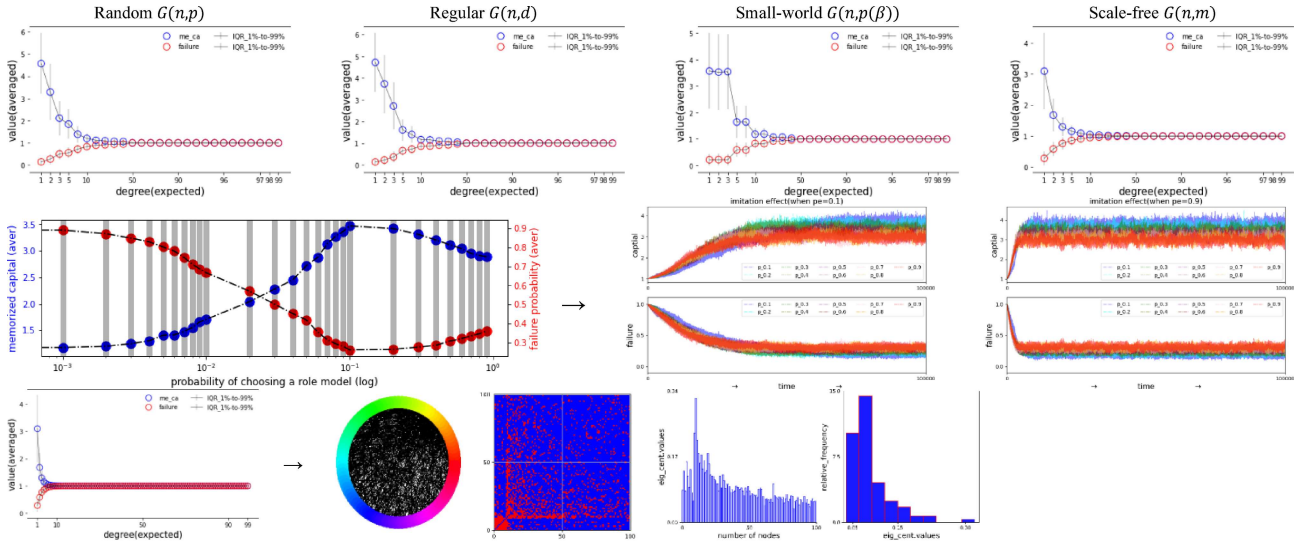

Increased simulation: memory (m_e = 0.9), exploration (p_e = 0.05), imitation (p_r = 0.1), time step (t = 50,000)

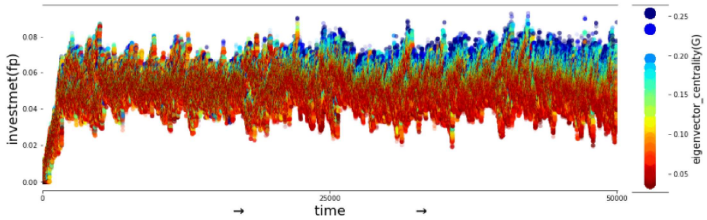

average investment (f_p) 0.051

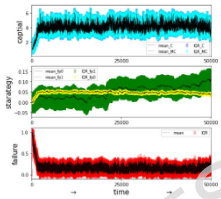

average me_ca 4.106
average failure 0.157

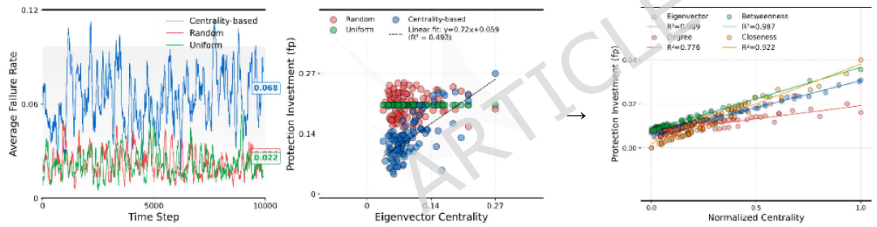

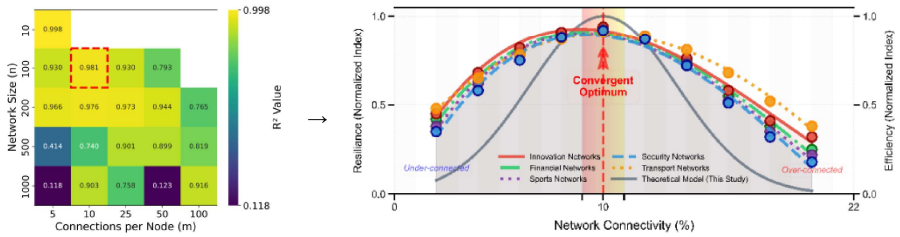

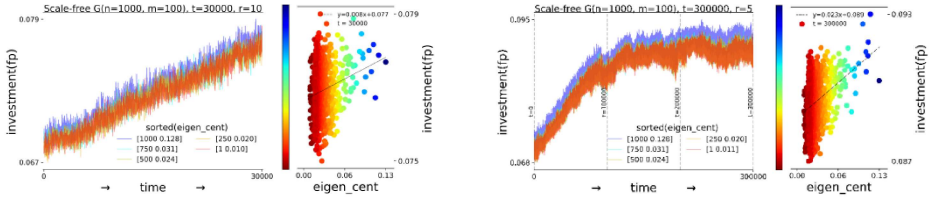

Main parameter: $n = 100$, $m = 10$, memory ($m_e = 0.9$), exploration ($p_e = 0.05$), imitation ($p_r = 0.1$), time step ($t = 300{,}000$)

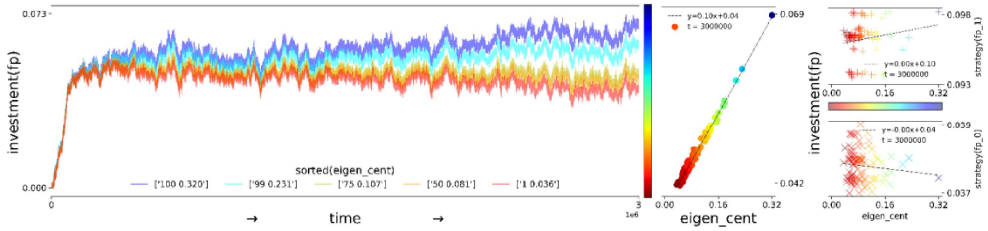

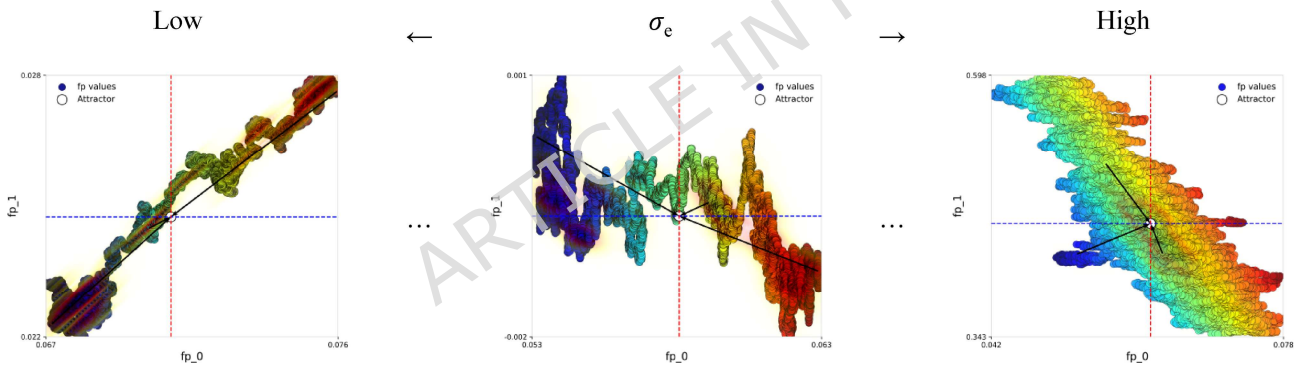

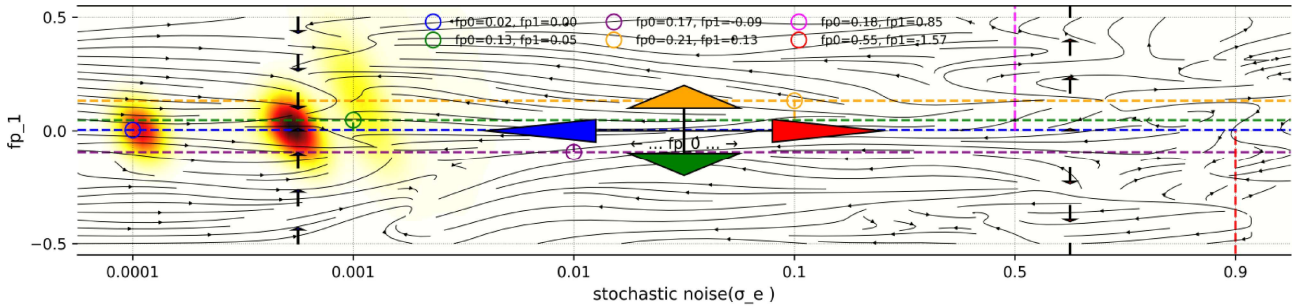

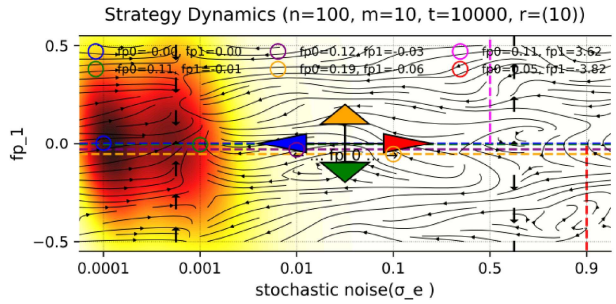

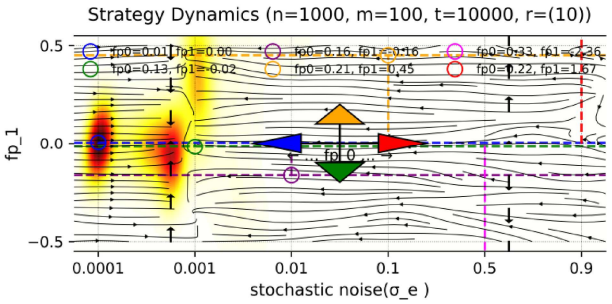

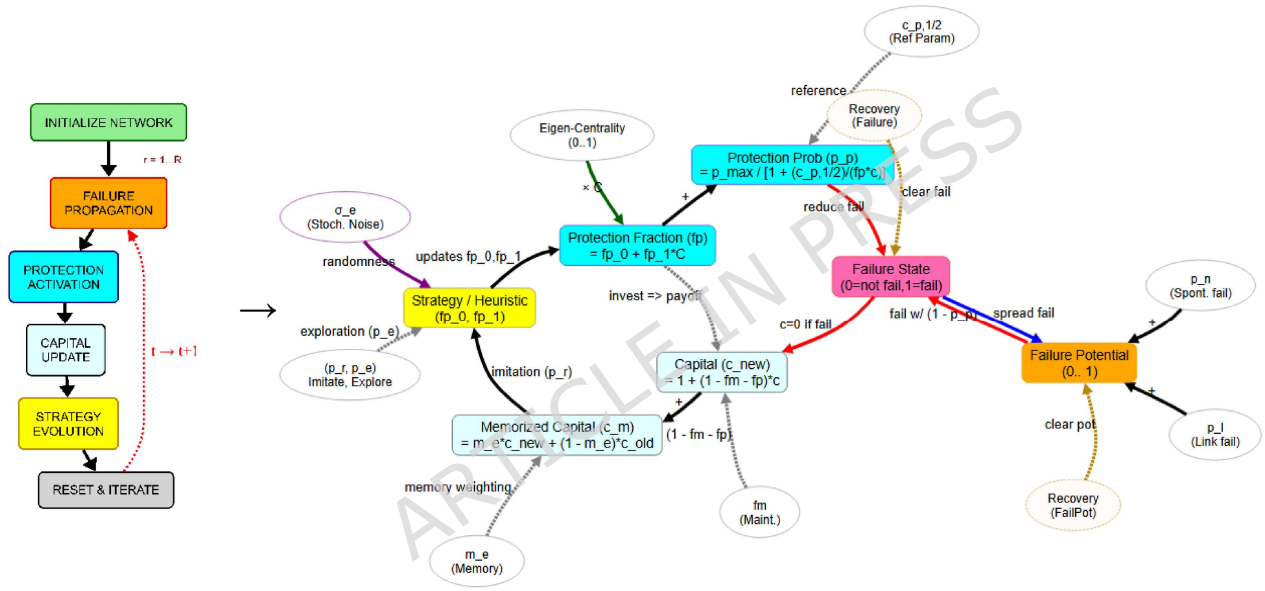

Centrality-Based Heuristics for Systemic Risk Management